AIAA JOURNAL
Vol. 49, No. 7, July 2011

Time-Domain Simulations of Outdoor Sound Propagation with Suitable Impedance Boundary Conditions

Didier Dragna,* Benjamin Cotté,† and Philippe Blanc-Benon‡
École Centrale de Lyon, 69134 Écully Cedex, France
and
Franck Poisson§
Société Nationale des Chemins de fer Français, 75379 Paris Cedex 08, France

DOI: 10.2514/1.J050636

Finite difference time-domain methods are attractive for the study of broadband outdoor noise propagation, because they can accurately take into account both atmospheric and ground effects. Moreover, these methods allow moving sound sources to be modeled, which can be interesting in the context of transportation noise. A recently proposed method to obtain an impedance boundary condition is implemented in a linearized Euler equations solver. A long-range propagation configuration in a two-dimensional geometry is studied in homogeneous conditions and in downward-refracting conditions with an impedance ground over a distance of 500 m. Two impedance models corresponding to a grassy ground and to a snow-covered ground are considered. Numerical results are compared in the time domain to an analytical solution in homogeneous conditions and to results from a ray-tracing code in downward-refracting conditions. Near the ground, surface waves are detected in the two cases and are the dominant arrivals in the homogeneous case.

Nomenclature

B_x = Gaussian half-width, m
c = speed of sound, m/s
c_0 = reference speed of sound, m/s
d_L = porous layer thickness, m
$\mathbf{E}, \mathbf{F}, \mathbf{H}, \mathbf{S}$ = vectors in linearized Euler equations
f = frequency, Hz
i = imaginary unit, $\exp(-i\omega t)$ convention
$Im[\,]$ = imaginary part
k_L = wave number in porous layer, m^{-1}
k_S = vertical wave number of surface wave, m^{-1}
k_0 = acoustic wave number, m^{-1}
p = acoustic pressure in time domain, Pa
$\hat{p}$ = acoustic pressure in frequency domain, Pa.s
Q = mass source, s^{-1}
Q_B = equivalent point source strength of Gaussian pulse, $\mathrm{Pa} \cdot \mathrm{s}$
$\mathbf{R}$ = external forces vector (R_x, R_z)
$Re[\,]$ = real part
R_1 = distance between source and receiver, m
R_2 = distance between image source and receiver, m
S = number of first-order systems in impedance approximation
t = time, s
$\mathbf{U}$ = unknown vector in linearized Euler equation
$\mathbf{v}$ = acoustic velocity vector (v_x, v_z)
v_n = velocity component normal to impedance surface in time domain, m/s
$\hat{v}_n$ = velocity component normal to impedance surface in frequency domain, m
$\mathbf{V_0}$ = mean flow vector (V_{0x}, V_{0z})
x, z = Cartesian coordinates
Z = characteristic impedance, $\mathrm{kg/m^2/s}$
Z_S = rational approximation of characteristic impedance, $\mathrm{kg/m^2/s}$
z_S = height of source, m
β = normalized admittance
Δt = time step, s
Δx = spatial mesh size, m
ρ_0 = air density, $\mathrm{kg/m^3}$
σ_e = effective flow resistivity, $\mathrm{Pa.s/m^2}$
ω = angular frequency, $\mathrm{rad.s^{-1}}$

Subscripts

D = direct wave
R = reflected wave
S = surface wave

I. Introduction

RECENTLY, there has been an increased interest in the study of sound propagation in the atmosphere in connection with European regulations limiting aircraft noise in the proximity of airports. Besides, numerical solutions of the linearized Euler equations (LEEs) with finite difference time-domain (FDTD) techniques are becoming more and more popular [1,2] in the outdoor sound propagation community. Indeed, these methods have proved their ability to account for many effects [3], such as refraction due to mean wind or mean temperature profiles, scattering by turbulence, or effects of topography. Consequently, they are useful in the context of transportation noise, where acoustic sources are usually broadband and in motion. The applications are numerous, including noise due to aircraft taxiing or to aircraft engine ground running, wind turbine

---

Presented as Paper 2009-3306 at the 15th AIAA/CEAS Aeroacoustics Conference, Miami, FL, 11–13 May 2009; received 25 June 2010; revision received 23 November 2010; accepted for publication 4 February 2011.

*Ph.D. Student, Centre National de la Recherche Scientifique, Laboratoire de Mécanique des Fluides et d'Acoustique, Unité Mixte de Recherche 5509; didier.dragna@ec-lyon.fr.

†Postdoctoral Researcher, Centre National de la Recherche Scientifique, Laboratoire de Mécanique des Fluides et d'Acoustique, Unité Mixte de Recherche 5509; currently Assistant Professor, Department of Mechanical Engineering, École Nationale Supérieur de Technique Avancées ParisTech, 91761 Palaiseau Cedex, France; benjamin.cotte@ec-lyon.fr.

‡Senior Research Scientist, Centre National de la Recherche Scientifique, Laboratoire de Mécanique des Fluides et d'Acoustique, Unité Mixte de Recherche 5509; philippe.blanc-benon@ec-lyon.fr. Member AIAA.

§Research Engineer, Direction de l'Innovation et de la Recherche; franck.poisson@sncf.fr.

noise, and railway noise propagation. However, one of the main difficulties in time-domain methods is deriving impedance boundary conditions. Ground impedance models classically used in outdoor sound propagation studies have been obtained in the frequency domain, and most of them do not meet the necessary conditions for a model to be physically possible [4–6], which means that they cannot be directly translated into the time domain.

In the outdoor sound propagation community, several studies have aimed at modeling sound propagation over an impedance ground in the time domain using two different approaches. Some authors chose to add a porous layer to the computation domain and calculated sound propagation in the porous medium explicitly [1,7]. Following the original work of Tam and Auriault [8] and other works done in the community of duct acoustics to model the impedance of lining materials in the time domain [4,9–11], others developed time-domain boundary conditions (TDBCs) from classical ground impedance models, such as the phenomenological Zwikker and Kosten model [12,13]. This former approach was used by Cotté et al. [2], who proposed a TDBC for outdoor sound propagation based on a recursive convolution method originally developed in the context of electromagnetic propagation [14] and introduced in acoustics by Reymen et al. [11]. It was shown that this TDBC is accurate and computationally efficient [15].

The primary objective of this paper is to show that, with this TDBC, relatively complex phenomena due to ground effects can be accurately taken into account; in particular, the presence of surface waves is investigated because these waves depend strongly on the impedance of the ground. To do so, a long-range configuration in a two-dimensional (2-D) geometry in a stratified atmosphere over a distance of 500 m is presented. An initial Gaussian pulse is considered with frequency contents up to 800 Hz.

In Sec. II of this paper, the LEE solver is described briefly, then the method used to obtain the TDBC is summarized and applied to model a grassy ground and a snowy ground with the two-parameter Miki impedance model [5,16]. Afterward, the long-range propagation configuration is studied. In Sec. III, homogeneous conditions are considered and the numerical results are compared in the time domain to an analytical solution. The waveforms obtained with the two different impedance models are presented. Finally, Sec. IV deals with propagation in downward-refracting conditions with a logarithmic sound speed profile. A comparison is made between the waveforms obtained with the two impedance ground surfaces and those obtained with the rigid ground surface. Ray-tracing calculations are considered to explain the wave arrivals, and the presence of a surface wave similar to the one that exists in homogeneous conditions is discussed.

II. Time-Domain Boundary Condition for a Linearized Euler Equations Solver

A. Linearized Euler Equations Solver

The LEEs are obtained by linearizing the fluid mechanics equations around a mean flow of density ρ_0, pressure P_0, and velocity $\mathbf{V_0} = (V_{0x}, V_{0z})$. The acoustic velocity $\mathbf{v} = (v_x, v_z)$ and the acoustic pressure p are then given by [17]

$$\frac{\partial p}{\partial t} + \mathbf{V_0} \cdot \nabla p + \rho_0 c^2 \nabla \cdot \mathbf{v} = \rho_0 c^2 Q \tag{1}$$

$$\rho_0 \frac{\partial \mathbf{v}}{\partial t} + \rho_0 (\mathbf{V_0} \cdot \nabla)\mathbf{v} + \rho_0 (\mathbf{v} \cdot \nabla)\mathbf{V_0} + \nabla p = \mathbf{R} \tag{2}$$

In Eqs. (1) and (2), t denotes the time, c is the sound speed in the air, and Q and $\mathbf{R}$ represent, respectively, a mass source and external forces. To get these equations, the air is assumed to be an ideal gas and terms of higher or equal order than $|\mathbf{v}|^2/c^2$ have been disregarded.

For numerical purpose, these equations can be written in a conservative form. In this paper, only 2-D configurations are considered. The LEEs are then written in the following conservative form:

$$\frac{\partial \mathbf{U}}{\partial t} + \frac{\partial \mathbf{E}}{\partial x} + \frac{\partial \mathbf{F}}{\partial z} + \mathbf{H} = \mathbf{S} \tag{3}$$

where the unknown vector $\mathbf{U}$ is chosen here as $[p, \rho_0 v_x, \rho_0 vz]^T$. To obtain the flux vectors $\mathbf{E}$, $\mathbf{F}$, $\mathbf{H}$, and $\mathbf{S}$, Eq. (1) is rewritten under the form

$$\frac{\partial p}{\partial t} + \nabla \cdot (p\mathbf{V_0}) - p\nabla \cdot \mathbf{V_0} + \nabla \cdot (\rho_0 c^2 \mathbf{v}) - \nabla(\rho_0 c^2) \cdot \mathbf{v} = \rho_0 c^2 Q \tag{4}$$

Under the assumption of an ideal gas, the sound speed verifies $c^2 = \gamma P_0/\rho_0$, where γ denotes the ratio of specific heats. The relation $\nabla(\rho_0 c^2) \cdot \mathbf{v} = \nabla(\gamma P_0) \cdot \mathbf{v}$ is then obtained. In the case of a moving inhomogeneous atmosphere, ∇P_0 is in the order $|\mathbf{v}|^2/c^2$ [17]. Thus, the term $\nabla(\rho_0 c^2) \cdot \mathbf{v}$, which is proportional to ∇P_0, should be ignored in Eq. (4). Moreover, following Ostashev et al. [17], it can be shown that $\nabla \cdot \mathbf{V_0} \sim |\mathbf{v}|^3/c^2 L$, where L is the length scale of variations in the density ρ_0. As a result, the term $-p\nabla \cdot \mathbf{V_0}$ is also neglected in Eq. (4). For the equation on $\rho_0 \mathbf{v}$, let us consider the equation for the mean density without source term

$$\frac{\partial \rho_0}{\partial t} + \mathbf{V_0} \cdot \nabla \rho_0 + \rho_0 \nabla \cdot \mathbf{V_0} = 0 \tag{5}$$

From Eqs. (2) and (5), the following relation is then obtained:

$$\frac{\partial \rho_0 \mathbf{v}}{\partial t} + (\mathbf{V_0} \cdot \nabla)\rho_0 \mathbf{v} + \rho_0 (\mathbf{v} \cdot \nabla)\mathbf{V_0} + (\nabla \cdot \mathbf{V_0})\rho_0 \mathbf{v} + \nabla p = \mathbf{R} \tag{6}$$

Finally, the term $(\mathbf{V_0}.\nabla)\rho_0 \mathbf{v}$ is rearranged and, after neglecting terms proportional to $\nabla \cdot \mathbf{V_0}$, the following expression is obtained for the flux vectors:

$$\mathbf{E} = \begin{pmatrix} V_{0x} p + \rho_0 c^2 v_x \\ V_{0x} \rho_0 v_x + p \\ V_{0x} \rho_0 v_z \end{pmatrix}, \qquad \mathbf{F} = \begin{pmatrix} V_{0z} p + \rho_0 c^2 v_z \\ V_{0z} \rho_0 v_x \\ V_{0z} \rho_0 v_z + p \end{pmatrix}$$
$$\mathbf{H} = \begin{pmatrix} 0 \\ \rho_0 \mathbf{v} \cdot \nabla V_{0x} \\ \rho_0 \mathbf{v} \cdot \nabla V_{0z} \end{pmatrix}, \qquad \mathbf{S} = \begin{pmatrix} \rho_0 c^2 Q \\ R_x \\ R_z \end{pmatrix} \tag{7}$$

The LEEs are solved using low-dispersion and low-dissipation explicit numerical schemes developed in the computational aeroacoustics community [18–21]. Optimized finite difference schemes and selective filters over 11 points are used for spatial derivation and grid-to-grid oscillations removal, respectively. These schemes allow us to accurately calculate acoustic wavelengths down to five or six times the spatial mesh size [2,22]. For the interior points, which are the ones separated by at least five points from the boundary, the centered fourth-order finite difference scheme of Bogey and Bailly [18] and the centered sixth-order selective filter of Bogey et al. [21] are used. For the boundary, which is the five extreme points in each direction, the 11-point noncentered finite difference schemes and selective filters of Berland et al. [20] are chosen. A filtering coefficient of 0.2 is taken for all selective filters, except at the extreme points where a filtering coefficient of 0.01 is chosen. This last filter is needed when a large number of time iterations (greater than 10,000) is performed [22]. The optimized six-stage Runge–Kutta algorithm proposed by Berland et al. [19], called RK-46L, is used for time integration.

The TDBC presented in the next subsection is applied at the ground boundary ($z = 0$ m). Its implementation has been described in detail in Cotté et al. [2] and will be summarized in Sec. II.B. The radiation boundary conditions of Tam and Dong [23] are implemented at the other boundaries. They are applied to the last three rows at each boundary point. The origin used for these boundary conditions is located on the ground at the source abscissa.

B. Time-Domain Impedance Boundary Conditions

Let $\hat{p}(\omega)$ and $\hat{v}_n(\omega)$ be, respectively, the Fourier transform of the acoustic pressure $p(t)$ and of the component of particle velocity normal to the interface between the ground and the air $v_n(t)$, where ω denotes the angular frequency. The characteristic impedance $Z(\omega)$ is defined in the frequency domain by the relation $\hat{p}(\omega) = Z(\omega)\hat{v}_n(\omega)$. To translate a frequency-domain impedance boundary condition to the time domain, the definition of impedance has to be extended to the whole complex frequency plane [4]. Using the $\exp(-i\omega t)$ convention, this leads to these necessary conditions for an impedance model to be physically possible [4]: 1) the causality condition, where

$$Z(\omega) \text{ is analytic and nonzero in } Im(\omega) > 0 \tag{8}$$

2) the reality condition, where

$$Z^*(\omega) = Z(-\omega) \tag{9}$$

and 3) the passivity condition, where

$$Re[Z(\omega)] \geq 0 \tag{10}$$

where $*$ means "complex conjugate of," and $Re[]$ means "real part of." The causality condition implies that the real and imaginary parts of the impedance are related by a Hilbert transform [5,6,24].

The impedance boundary condition can be written in the time domain under the form

$$p(t) = \int_{-\infty}^{+\infty} z(t - t')v_n(t')\,\mathrm{d}t' \tag{11}$$

where $z(t)$ is the inverse Fourier transform of the impedance $Z(\omega)$. The numerical computation of this convolution requires a great computational effort. To avoid this calculation, the recursive convolution method, introduced by Luebbers and Hunsberger [14] in the context of electromagnetic propagation through dispersive media, can be used. First, following a method proposed by Fung and Ju [10] and Reymen et al. [11], the characteristic impedance is approximated as a sum of first-order systems:

$$Z(\omega) \approx Z_S(\omega) = \sum_{k=1}^{S} \frac{A_k}{\lambda_k - i\omega} \tag{12}$$

with λ_k as the poles, A_k as the corresponding coefficients, and S as the number of poles. If $\lambda_k \geq 0$ and $Re[Z_S(\omega)] \geq 0$, the impedance is guaranteed to be physically possible. With this form, the inverse Fourier transform of the impedance is given by

$$z(t) = \sum_{k=1}^{S} A_k \exp(-\lambda_k t)H(t) \tag{13}$$

where $H(t)$ is the Heaviside function. Inserting $z(t)$ in Eq. (11) and considering the discretized variables $p^{(m)} = p(m\Delta t)$ and $v_n^{(m)} = v_n(m\Delta t)$, with Δt as the time step, the following TDBC is obtained:

$$p^{(m)} = \sum_{k=1}^{S} A_k \phi_k^{(m)} \tag{14}$$

where ϕ_k are called accumulators. Assuming that v_n is constant over a time step, these accumulators are given by the recursive formula,

$$\phi_k^{(m)} = v_n^{(m)} \frac{1 - e^{-\lambda_k \Delta t}}{\lambda_k} + \phi_k^{(m-1)} e^{-\lambda_k \Delta t} \tag{15}$$

In this TDBC, S accumulators are needed, with only two storage locations per accumulator.

Cotté et al. [2] compared different methods to identify the coefficients A_k and λ_k of Eq. (12) and proposed an optimization method in the frequency domain that ensures accurate numerical results [2,15]. Two impedance models will be investigated here:

1) The Miki impedance model of a semi-infinite ground layer [5] will be investigated, which is physically possible:

$$Z_M/\rho_0 c_0 = 1 + 0.06999(f/\sigma_e)^{-0.632} + i0.107(f/\sigma_e)^{-0.632} \tag{16}$$

with f as the frequency, c_0 as the reference sound speed of 340 m/s, and σ_e as the effective flow resistivity expressed in SI units,

2) A two-parameter impedance model will be investigated, which can be built on the basis of Eq. (16), considering a rigidly backed layer of thickness d_L. The characteristic impedance is then written [16] as

$$Z_L = iZ_M/\tan(k_L d_L) \tag{17}$$

where k_L is the complex wave number in the porous layer:

$$k_L = \frac{\omega}{c_0}\left[1 - 0.109\left(\frac{f}{\sigma_e}\right)^{-0.618} + i0.160\left(\frac{f}{\sigma_e}\right)^{-0.618}\right] \tag{18}$$

Two sets of coefficients A_k and λ_k are used in this paper and are given in Table 1. The first one is obtained with the Miki impedance model of a semi-infinite ground layer with an effective flow resistivity of 100 kPa · s · m^{-2}, typical for grassy grounds, and so it will be denoted as grass. The second one corresponds to a rigidly backed layer of thickness 0.1 m with an effective flow resistivity of 10 kPa · s · m^{-2}, typical for snow grounds [25]. Even if a four-parameter impedance model is a better modelization of snow grounds, the single-parameter model can give reasonably good estimates [26]. Thus, this model will be denoted as snow. The coefficient identification method is performed on the frequency band from 50 to 1200 Hz. The real and imaginary parts of the impedance models are plotted in Fig. 1. The solid line corresponds to the Miki model, and the dots correspond to the fit obtained using the frequency domain approximation. The frequency band from 50 to 1200 Hz is represented by vertical lines. It can be seen that the real and imaginary parts of the impedance model are well approximated in the band of interest in both cases. It should also be noticed that the real part of the impedance model is positive [passivity condition; see Eq. (10)], as well as the imaginary part. It will be seen in Sec. III.B that these conditions are of great importance for surface waves.

In Sec. IV, a rigid ground surface will also be considered. In this case, the boundary condition at the ground surface is just $v_n = 0$.

C. Numerical Simulation in Stratified Atmosphere

For all simulations presented in this paper, a uniform mesh in both directions of size $\Delta x = 0.05$ m is chosen. The Courant–Friedrichs–Lewy number equal to $c_0\Delta t/\Delta x$ is fixed at one. The domain size is approximately 500 m in the x direction and 100 m in the z direction. There are about 22 million points in the calculation domain. The calculation is performed over 11,000 time iterations to ensure that the pulse has left the computational domain. A stratified atmosphere is considered with the sound speed $c(z)$ being a function of height.

In the numerical simulation, an initial Gaussian pressure distribution is considered:

Table 1 Coefficients A_k and λ_k used for TDBC[a]

	Grass	Snow
σ_e, kPa · s · m^{-2}	100	10
d_L, cm	∞	10
A_1	$1.414390450609 \times 10^6$	$-2.387726592746 \times 10^5$
A_2	$1.001354674975 \times 10^6$	$1.305064908175 \times 10^6$
A_3	$-3.336020206713 \times 10^6$	$9.117487447153 \times 10^4$
A_4	$5.254549668250 \times 10^6$	$-4.401629389144 \times 10^6$
A_5	$3.031704943714 \times 10^7$	$2.711843630923 \times 10^7$
λ_1	$5.233002301836 \times 10^1$	$1.446366202093 \times 10^0$
λ_2	$4.946064975401 \times 10^2$	$2.130280276492 \times 10^0$
λ_3	$1.702517657290 \times 10^3$	$1.263750200412 \times 10^3$
λ_4	$1.832727486745 \times 10^3$	$6.531094031584 \times 10^3$
λ_5	$3.400000000000 \times 10^4$	$2.719883119792 \times 10^4$

[a] The set of coefficients called grass corresponds to the Miki impedance model for a semi-infinite ground layer of effective flow resistivity 100 kPa · s · m^{-2}. It was referred to as "OF v1" in [2]. The second set, called snow, corresponds to the Miki model of a rigidly backed layer of thickness 0.1 m and of effective flow resistivity 10 kPa · s · m^{-2}.

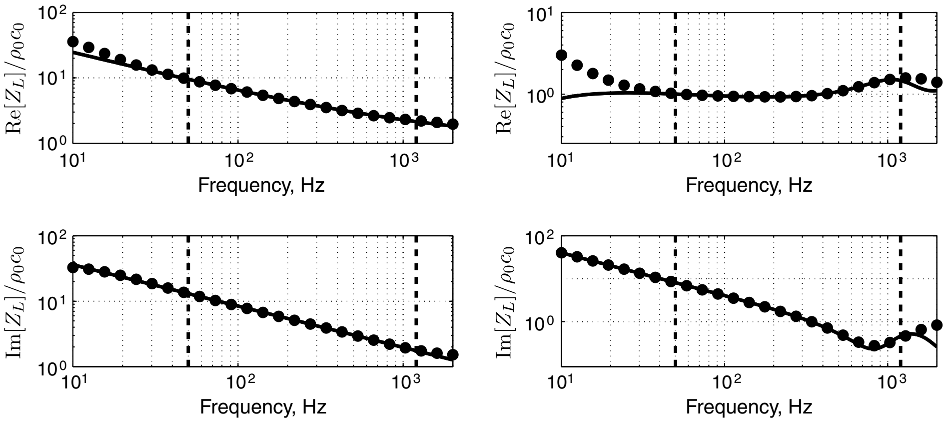

a) Grass **b) Snow**

Fig. 1 Real and imaginary parts of the normalized impedance for a) a semi-infinite ground layer with an effective flow resistivity 100 kPa · s · m^{-2} and b) a rigidly backed layer of thickness 0.1 m and of effective flow resistivity 10 kPa · s · m^{-2}.

$$p(x,z,t=0) = S_0 \exp\left(-\ln 2\,\frac{x^2+(z-z_S)^2}{B_x^2}\right) \tag{19}$$

where z_S is the height of the source and the parameter S_0 is set arbitrarily to 1 Pa. All along this article, the pressure will be normalized by S_0. The Gaussian half-width is set to $B_x = 5\Delta x$. The shape of the Gaussian pulse is plotted in Fig. 2 for $\Delta x = 0.05$ m.

First, the frequency content of this source has to be determined. To do so, we consider the propagation of this initial pressure distribution in free field for a homogeneous atmosphere with $c = c_0$. In this case, the analytical solution is given by Tam and Webb [27]:

$$p(r,t) = \frac{S_0 B^2}{2}\int_0^{+\infty} \exp\left(\frac{-k^2B^2}{4}\right)\cos(kc_0t)J_0(kr)k\,\mathrm{d}k \quad H(t) \tag{20}$$

where r is the distance to the source, J_0 is the Bessel function of order zero, and $B^2 = B_x^2/\ln 2$. The acoustic pressure for the outgoing wave can then be written as an inverse Fourier transform times the Heaviside function:

$$p(r,t) = \frac{1}{2\pi}\int_{-\infty}^{+\infty} \hat{p}(r,\omega)\exp(-i\omega t)\,\mathrm{d}\omega \quad H(t) \tag{21}$$

The pressure in the frequency domain $\hat{p}$ corresponds to the 2-D Green function [24] times a factor that depends only on the frequency:

$$\hat{p}(r,\omega) = -\frac{i}{4}Q_B(\omega)H_0^{(1)}(k_0r) \tag{22}$$

where $H_0^{(1)}$ is the Hankel function, $k_0 = 2\pi f/c_0$ is the acoustic wave number, and Q_B is an equivalent point source strength given by

$$Q_B(\omega) = ik_0\frac{S_0\pi B^2}{c_0}\exp\left(-\frac{k_0^2B^2}{4}\right) \tag{23}$$

The modulus of the equivalent point source strength is plotted in Fig. 2. It can be noticed that this starter has a broadband spectrum with significant frequency content up to 800 Hz. In the next simulations, the source is located at $(0, z_S)$, with the source height z_S set to $40\Delta x = 2$ m.

III. Homogeneous Atmosphere

In this section, a homogeneous atmosphere is considered: the sound speed profile is then $c(z) = c_0 = 340$ m/s. Two simulations are performed with the impedance models described in Sec. II.B and with the initial pressure distribution presented in Sec. II.C. In Fig. 3, the waveforms obtained in the two cases are plotted at 500 m. It can be seen that their shapes are quite different due to the ground effect. For the two impedances, two short arrivals and a long tail component can be distinguished. The first arrival is the same and corresponds to the direct wave. The second arrival is related to the reflected wave and seems mixed near the ground with the low-frequency tail. It will be shown that this tail is due to what is called surface wave in the literature.

A. Surface Wave Component

The surface wave contribution appears in the analytical calculation of the propagation of a point source above a flat impedance ground in

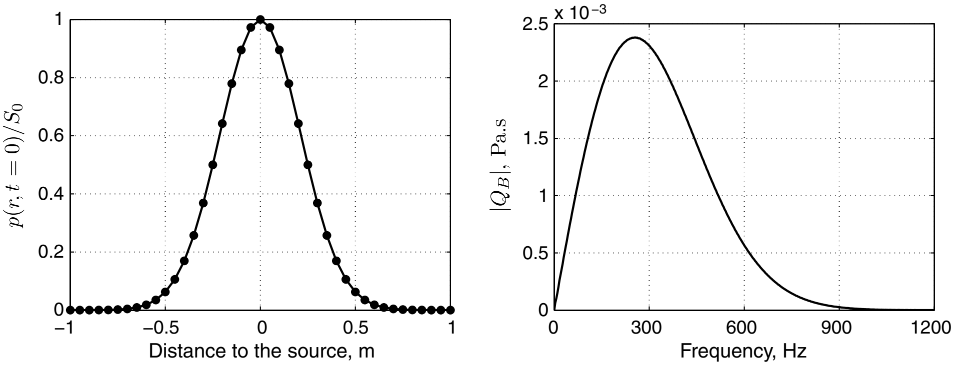

a) **b)**

Fig. 2 Gaussian pulse: a) initial pressure distribution $p(r,t=0)/S_0$ versus the distance to the source r and b) the modulus of the equivalent point source strength Q_B.

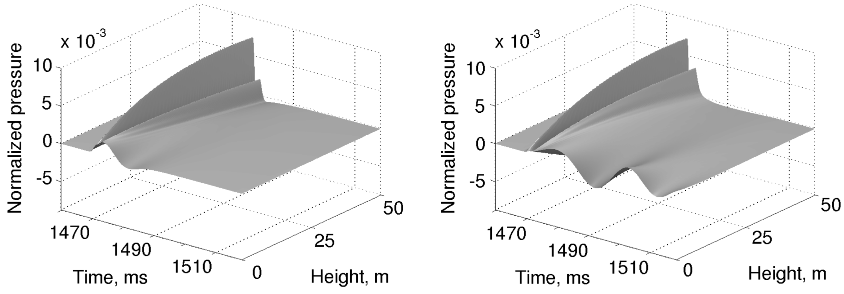

a) Grass **b) Snow**

Fig. 3 Pressure waveforms obtained at distance $x = 500$ m for a homogeneous atmosphere: a) grass impedance model and b) snow impedance model. Height of source is 2 m.

homogeneous conditions [28]. It physically represents a separated wave propagating close to the impedance surface. Surface waves have several important properties. The amplitude of surface waves decays exponentially with height. In the three-dimensional (3-D) case, it also decays with the square root of range, whereas the other waves decay linearly with range. For long ranges and receivers close to the ground, it could then become the major contribution to the acoustic pressure. Surface waves also exist in downward-refracting conditions. Indeed, Waxler et al. [29], have shown that the lowest-order mode in modal expansions is related to the surface wave. One can also cite the work of Zorumski and Willshire [30], who have shown that, assuming an exponential wind velocity profile with a low-wind approximation, a wave related to the surface wave in homogeneous conditions was a part of the solution. Existence of surface wave has been verified in outdoor sound experiments by Albert [31], who studied propagation of acoustic pulses generated by pistol shots above a snow layer with similar physical characteristics as the ones used here for the snow impedance model.

In 2-D geometry, the analytical expression of the surface wave for a monopole of unit amplitude is given by [32]

$$\hat{p}_S(x,z,\omega) = \frac{k_S}{\sqrt{k_0^2 - k_S^2}} \exp[i\sqrt{k_0^2 - k_S^2}x) \exp(-ik_S(z + z_S)] \tag{24}$$

where $k_S = k_0\beta$ is the vertical wave number of the surface wave and β is the normalized admittance of the ground defined by $\beta = \rho_0 c_0/Z$. From Eq. (24), it can be noted that the decay with the height of the surface wave depends on the height of the receiver but also on the height of the source. It can also be noticed that, in 2-D, the surface wave is a plane wave, while in 3-D, it can be seen as a cylindrical wave. Otherwise, it has been shown that the surface wave exists under some conditions: Enflo and Enflo [33] have shown that the real and imaginary parts of the impedance must both be positive. As noticed in Sec. II.B, the condition is verified for the two impedance models.

B. Comparison in Time Domain with Analytical Model

The numerical solution is now compared with an analytical solution in the time domain. The scheme of the problem is depicted in Fig. 4. The analytical calculation can be found in Salomons et al. [1]. The acoustic pressure is written under the form

$$\hat{p}(x,z,\omega) = \hat{p}_D(x,z,\omega) + \hat{p}_R(x,z,\omega) + \hat{p}_S(x,z,\omega) \tag{25}$$

where $\hat{p}_D$ and $\hat{p}_R$ are, respectively, the direct and the reflected waves, and $\hat{p}_S$ is the surface wave for which the expression is given in Eq. (24). Assuming that the passivity condition is fulfilled ($Re[Z(\omega)] \geq 0$), the direct wave $\hat{p}_D$ and the reflected wave $\hat{p}_R$ are then given by [1]

$$\hat{p}_D(x,z,\omega) = -\frac{i}{4} H_0^{(1)}(k_0 R_1) \tag{26}$$

$$\hat{p}_R(x,z,\omega) = -\frac{i}{4} H_0^{(1)}(k_0 R_2) + \frac{ik_S}{2}\int_0^{+\infty} \exp(-k_S q) H_0^{(1)}(k_0 R_q)\,\mathrm{d}q - \hat{p}_S(x,z,\omega) \tag{27}$$

where $R_1 = \sqrt{x^2 + (z - z_S)^2}$ is the distance between the source and the receiver, $R_2 = \sqrt{x^2 + (z + z_S)^2}$ is the distance between the image source and the receiver, and R_q is a parameter given by $R_q = \sqrt{x^2 + (z + z_S + iq)^2}$. Note that the surface wave is extracted from the integral term. This expression is the same as the one obtained by Di and Gilbert [34] with the replacement of the 3-D Green function by the 2-D Green function. The calculation of the integral term used a simple trapezoidal rule. The upper limit of the integral is set to $10/Re[k_S]$, and the integrand is discretized over 500 points. The analytical pressure in the time domain can then be obtained for each wave individually by the formula

$$p(x,z,t) = \frac{1}{2\pi}\int_{-\infty}^{+\infty} Q_B(\omega)\hat{p}(x,z,\omega)\exp(-i\omega t)\,\mathrm{d}\omega \tag{28}$$

which can be numerically calculated by discrete Fourier transform.

In Fig. 5, the analytical waveforms are plotted in the two cases for a receiver located at a height of 5 m. It can be seen that the short peaks are due to the direct and reflected waves; furthermore, the direct wave is the same in the two cases, while the reflected wave, which depends on the impedance, is slightly different. As expected, the surface wave has a low-frequency content. It is worthwhile to notice that the surface wave has a noncausal behavior; indeed, as noted by Albert [31], the waveform of the surface wave begins before the direct wave arrival. Actually, this noncausal part of the surface wave is exactly canceled by the reflected wave, as can be observed in Fig. 5.

Figure 6 compares the waveform obtained by numerical calculation and those obtained by the total analytical solution for receivers at different heights. The two waveforms are almost indistinguishable. The surface wave is also represented, and it can be seen that the low-frequency tail corresponds well with the surface wave. The waveform of the surface wave is very different in the two cases, while for the snow model, the oscillations decay slowly in time, and for the grass model, the surface wave oscillations decay

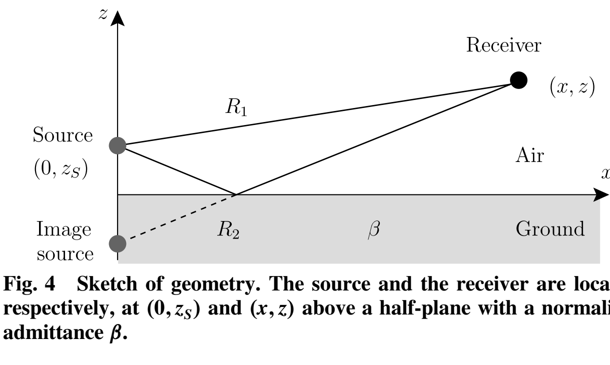

Fig. 4 Sketch of geometry. The source and the receiver are located, respectively, at $(0, z_S)$ and (x, z) above a half-plane with a normalized admittance β.

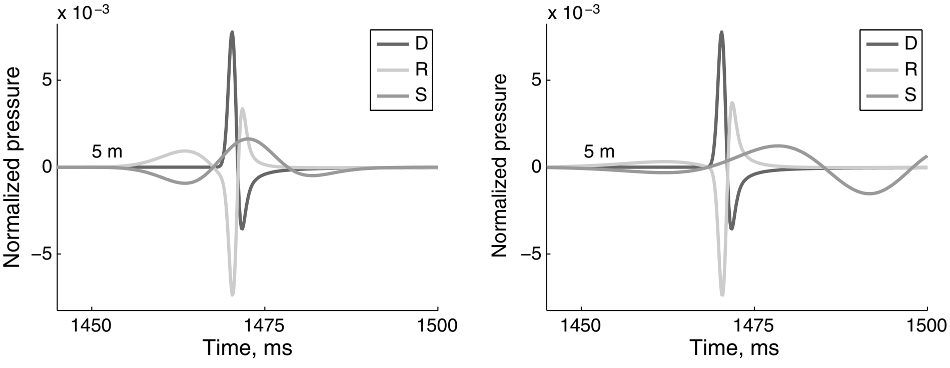

a) Grass b) Snow

Fig. 5 Analytical waveforms of pressure obtained at distance $x = 500$ m for a receiver 5 m above ground: a) grass impedance model and b) snow impedance model. D, R, and S stand for direct wave, reflected wave, and surface wave, respectively.

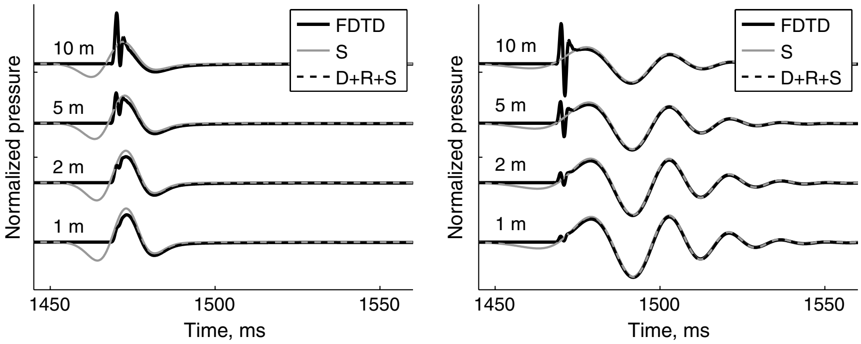

a) Grass b) Snow

Fig. 6 Comparison of waveforms of pressure obtained at distance $x = 500$ m for different heights with the numerical solver (solid line) and with the analytical solution (dashed line): a) grass impedance model and b) snow impedance model.

more rapidly. Finally, the amplitude of the peaks corresponding to the direct wave and to the reflected wave is weak near the ground due to grazing incidence and increases with height as opposed to the surface wave amplitude.

IV. Downward-Refracting Conditions

In this section, propagation of sound in a stratified downward-refracting atmosphere is studied. The impedance models of a grassy ground and of a snowy ground, presented in Sec. II.B, are used in the TDBC. A logarithmic sound speed profile is now considered:

$$c(z) = c_0 + a_c \log(1 + z/z_0) \tag{29}$$

with $c_0 = 340$ m/s, $a_c = 1$ m/s, and $z_0 = 0.1$ m. This sound speed profile is a characteristic of a neutral atmosphere [1].

A. Comparison of Waveforms

Pressure waveforms obtained at a distance $x = 500$ m from the source for the two impedance cases and for receivers located at heights up to 50 m are plotted on Fig. 7. These waveforms are more complex than those obtained in homogeneous conditions (see Fig. 3). Indeed, additional arrivals are observed compared with the homogeneous case. Moreover, the amplitude of the pressure is larger near the ground due to atmospheric refraction. In particular, a large amplification can be seen for the snow impedance model (Fig. 7b) for receiver heights of about 5 m and at $t = 1457$ ms. Indeed, due to refraction, a surface waveguide is created [35].

To highlight the ground effect and the waveguide effect close to the ground, a numerical simulation has been performed with a perfectly reflecting ground surface. Pressure waveforms, obtained in this case at a distance $x = 500$ m from the source, are shown on Fig. 8. It can be noted that the maximum of pressure is located on the ground ($z = 0$ m) for wave arrivals at about $t = 1461$ ms, and that its value is approximately four times greater than the one in the impedance

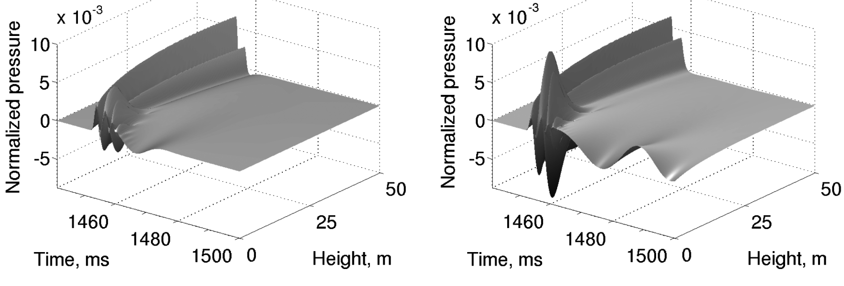

a) Grass b) Snow

Fig. 7 Pressure waveforms obtained at distance $x = 500$ m for a downward-refracting atmosphere: a) grass impedance model and b) snow impedance model. Height of source is 2 m.

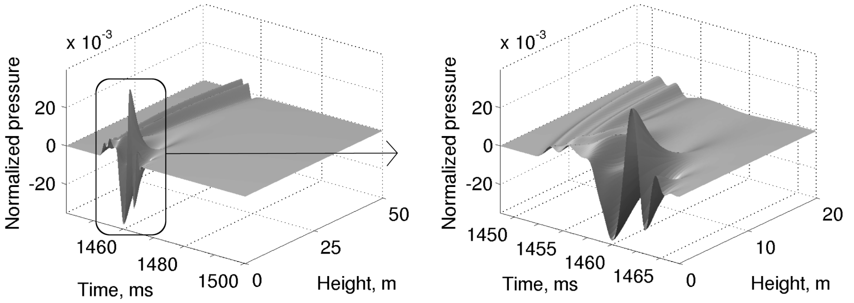

Fig. 8 Pressure waveforms obtained at distance $x = 500$ m for a downward-refracting atmosphere from a) $t = 1441$ ms to $t = 1500$ ms and b) $t = 1449$ ms to $t = 1467$ ms (zoom of Fig. 8a). Height of source is 2 m. Rigid ground surface is considered here.

cases. It can also be noticed that the pressure decreases rapidly with height. Thus, for heights greater than $z = 25$ m, only two wave arrivals can be clearly distinguished with arrival times between $t = 1451$ ms and $t = 1454$ ms and between $t = 1453$ ms and $t = 1456$ ms.

Besides, for the impedance cases, a long tail component, characteristic of a surface wave, can be seen after the first wave arrivals ($t > 1462$ ms) on the waveforms on Fig. 7. Its behavior is comparable to that observed on Fig. 3 for homogeneous conditions: it is a low-frequency contribution that vanishes slowly with time and that decays with height. In particular, for the snow impedance model, the oscillations of pressure near the ground are recovered (see Figs. 3b and 7b). On the contrary, for the rigid ground surface, the pressure is almost zero for $t > 1465$ ms. Thus, the long tail component does not exist for the rigid ground case.

B. Analysis with Ray-Tracing Calculation

It was shown by Cotté and Blanc-Benon [15,36] that a good agreement is found for the sound pressure level between the FDTD numerical simulations and calculations using a parabolic equation code through the frequency band of interest in the case of the grass impedance model. To clarify the different contributions, a good approach is to consider a ray-tracing calculation. Indeed, with this high-frequency method, based on the geometric acoustics approximation, the travel times along the rays can be calculated. By definition, sound rays are the tangent lines to the group velocity vector and represent the wavefront trajectories between the source and the receiver. For each receiver, the different eigenrays are determined by solving the classical eikonal equation using the method of characteristics (see, e.g., Candel [37]). The numerical integration uses the fourth-order Runge–Kutta algorithm. The condition of specular reflection is assumed at the boundary. In the ray-tracing calculation, the sound pressure at the receiver is the sum of all the ray contributions. The number of rays reaching the receiver has then to be determined. Note that, here, only arrival times of the eigenrays are considered, and acoustic levels are not calculated. To do so, the rays reaching receivers with a height of 2 m and with range from 0 to 550 m are calculated. Thereafter, they are arranged in groups according to the number m of reflections on the ground. Each group is then denoted as R_m. On Fig. 9b, the launch angles of these rays, denoted as θ, are plotted versus range. The case $\theta > 0$ (respectively, $\theta < 0$) corresponds to a ray initially propagating upward (respectively, downward). This figure shows that the number of eigenrays increases with distance. It can also be seen that, for $m > 1$, each group contains four rays. The group corresponding to $m = 1$ contains three rays, except for small propagation distances. Indeed, for a distance lower than 100 m, only two rays, which are the direct ray and the reflected ray, reach the receivers.

Now we focus on two propagation distances $x = 250$ m and $x = 500$ m in order to analyze the waveforms using the ray-tracing calculation for the grass impedance model. From Fig. 9b, it can then be seen that there are eight eigenrays for $x = 250$ m. They correspond to the direct ray R_0 ($\theta = 0.080$ rad), to the three rays R_1 that have been reflected one time on the ground ($\theta = -0.074$ rad, $\theta = 0.050$ rad, and $\theta = 0.074$ rad), and to the four rays R_2 that have been reflected two times on the ground ($\theta = -0.066$ rad, $\theta = -0.039$ rad, $\theta = 0.024$ rad, and $\theta = 0.039$ rad). For $x = 500$ m, there are 20 eigenrays with a maximum number of reflections on the ground equal to five. The corresponding eigenrays are represented in Fig. 10. Direct rays and eigenrays with one and two reflections are plotted with the same color as in Fig. 9b. Eigenrays with more than two reflections are plotted in light gray. The waveguide effect is clear; in particular, for $x = 500$ m, most of the eigenrays propagate close to the ground.

The arrival times associated with the eigenrays correspond with a good accuracy to the first extrema of pressure for both distances, as can be seen in Fig. 11. In detail, the first and second extrema correspond, respectively, to the direct ray and to the eigenray that has been reflected at the ground and has then reached the receiver. For $x = 250$ m, the others eigenrays have close arrival times and their contributions are mixed. For $x = 500$ m, the contributions of the direct ray and of the eigenrays with one and two reflections can be clearly identified on the waveforms. The contributions associated to the other eigenrays again have close arrival times and cannot be easily distinguished. Moreover, these eigenrays have been reflected

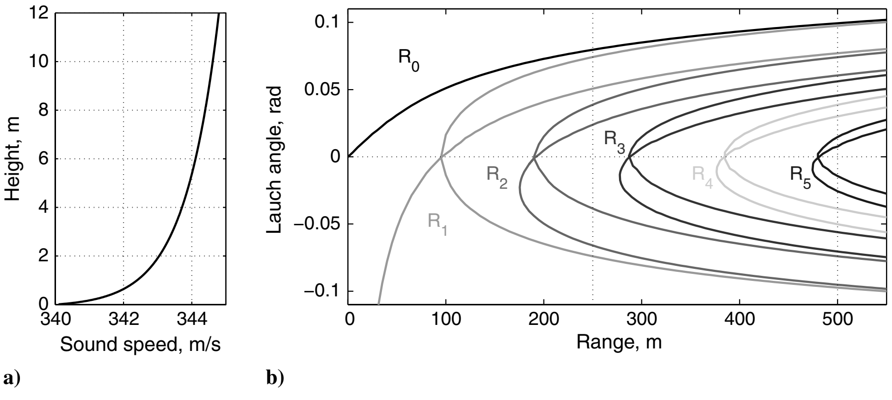

a) b)

Fig. 9 Parameters of the eigenrays: a) sound speed profile and b) launch angles calculated for receivers with a height of 2 m and a range from 0 to 550 m.

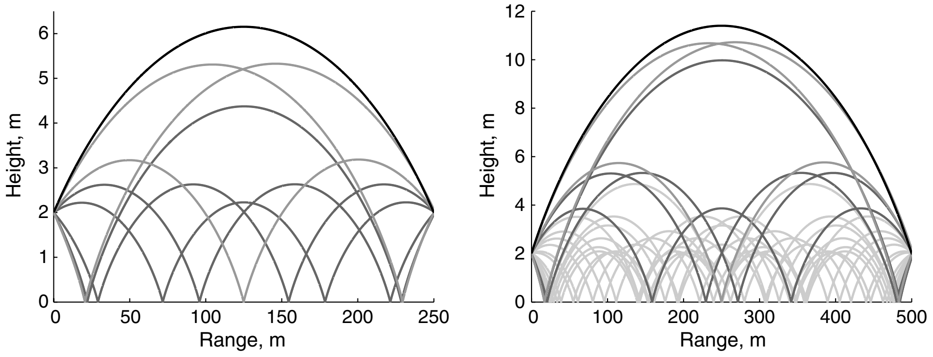

a) b)

Fig. 10 Eigenrays calculated for a receiver at $z = 2$ m and at a) $x = 250$ m and b) $x = 500$ m.

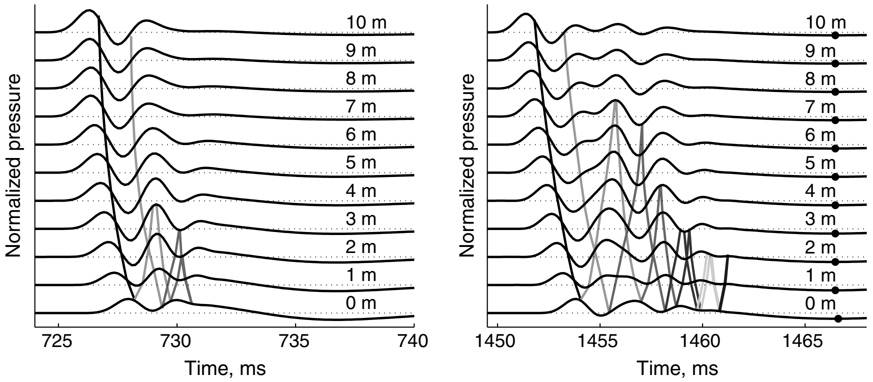

a) 250 m b) 500 m

Fig. 11 Normalized pressure $p(t)/S_0$ at a) $x = 250$ m and b) $x = 500$ m and at different heights (as labeled) in downward-refracting conditions ($a_c = +1$ m/s) for the grass impedance model.

several times on the impedance ground surface and carry less energy than the other ones.

In both cases, it can be emphasized that, for times long enough ($t = 735$ ms for $x = 250$ m and $t = 1465$ ms for $x = 500$ m), the pressure signal does not return to zero, unlike the case of the rigid ground surface. Moreover, this long tail component cannot be linked to any ray arrival, as can be seen on Fig. 11. This means that the long tail component does not correspond to a geometric arrival and may then be a surface wave component.

It has been seen in Sec. III.A that the surface wave decreases exponentially with height for a homogeneous atmosphere. In Fig. 12, the logarithm of the minimum of the long tail component, marked with dots in Fig. 11b for the grass case, is plotted versus height for the two impedance models. The fit obtained by the least-squares method is also plotted as a solid line. The exponential attenuation with height is clear in the two cases. All this evidence confirms that the long tail arrival is also due to a surface wave in the downward-refracting conditions.

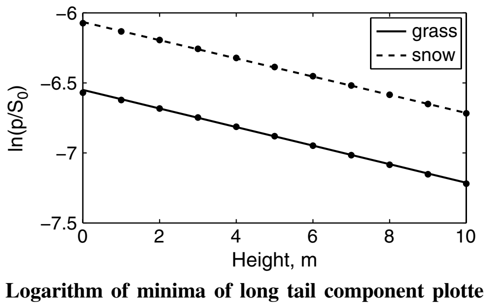

Fig. 12 Logarithm of minima of long tail component plotted versus height for two impedance models at a distance of 500 m.

V. Conclusions

In this paper, a general TDBC based on a recursive convolution method has been implemented in a LEE solver. The impedance of two types of ground has been derived with a method recently proposed on the frequency range from 50 to 1200 Hz. A 2-D long-range configuration in a stratified atmosphere has been studied over a distance of 500 m and with frequency contents up to 800 Hz. In homogeneous conditions, a very good agreement is obtained between numerical results and an analytical solution in the time domain. In downward-refracting conditions, the time arrivals of the different waves are found to be in close agreement with those given by a ray-tracing algorithm. In both cases, a surface wave component has been clearly identified; for the homogeneous case, it is the major contribution to the sound pressure near the ground. It has also been shown that the waveform of the surface wave component depends strongly on the impedance model. In the different outdoor sound propagation cases, the TDBC has proved to be efficient and has yielded accurate results. Further work will take into account effects of topography that, coupled with ground effect, can have a noticeable influence on sound propagation.

Acknowledgments

Support by the Centre National de la Recherche Scientifique and the Société Nationale des Chemins de fer Français is gratefully acknowledged. The authors would also like to thank Olivier Marsden for providing helpful comments on the manuscript. This work was granted access to the high-performance computing resources of Institut du Développement et des Ressources en Informatique Scientifique under the allocation 2010-022203 made by the Grand Equipement National de Calcul Intensif.

References

[1] Salomons, E. M., Blumrich, R., and Heimann, D., "Eulerian Time-Domain Model for Sound Propagation over a Finite-Impedance Ground Surface. Comparison with Frequency-Domain Models," *Acta Acustica United with Acustica*, Vol. 88, No. 4, 2002, pp. 483–492.

[2] Cotté, B., Blanc-Benon, P., Bogey, C., and Poisson, F., "Time-Domain Impedance Boundary Conditions for Simulations of Outdoor Sound Propagation," *AIAA Journal*, Vol. 47, No. 10, 2009, pp. 2391–2403. doi:10.2514/1.41252

[3] Bailly, C., and Juvé, D., "Numerical Solution of Acoustic Propagation Problems Using Linearized Euler Equations," *AIAA Journal*, Vol. 38, No. 1, 2000, pp. 22–29. doi:10.2514/2.949

[4] Rienstra, S. W., "Impedance Models in Time Domain Including the Extended Helmholtz Resonator Model," 12th AIAA/CEAS Aeroacoustics Conference, Cambridge, MA, AIAA Paper 2006-2686, 2006.

[5] Miki, Y., "Acoustical Properties of Porous Materials: Modifications of Delany–Bazley Models," *Journal of the Acoustical Society of Japan*, Vol. 11, No. 1, 1990, pp. 19–24.

[6] Berthelot, Y. H., "Surface Acoustic Impedance and Causality," *Journal of the Acoustical Society of America*, Vol. 109, No. 4, 2001, pp. 1736–1739. doi:10.1121/1.1352089

[7] Van Renterghem, T., and Botteldooren, D., "Numerical Simulation of the Effect of Trees on Downwind Noise Barrier Performance," *Acta Acustica United with Acustica*, Vol. 89, No. 5, 2003, pp. 764–778.

[8] Tam, C., and Auriault, L., "Time-Domain Impedance Boundary Conditions for Computational Aeroacoustics," *AIAA Journal*, Vol. 34, No. 5, 1996, pp. 917–923. doi:10.2514/3.13168

[9] Özyörük, Y., and Long, L., "A Time-Domain Implementation of Surface Acoustic Impedance Condition with and Without Flow," *Journal of Computational Acoustics*, Vol. 5, No. 3, 1997, pp. 277–296. doi:10.1142/S0218396X97000162

[10] Fung, K.-Y., and Ju, H., "Broadband Time-Domain Impedance Models," *AIAA Journal*, Vol. 39, No. 8, 2001, pp. 1449–1454. doi:10.2514/2.1495

[11] Reymen, Y., Baelmans, M., and Desmet, W., "Time-Domain Impedance Formulation Suited for Broadband Simulations," *13th AIAA/CEAS Aeroacoustics Conference*, Rome, AIAA Paper 2007-3519, 2007.

[12] Wilson, D. K., Collier, S. L., Ostashev, V. E., Aldridge, D. F., Symons, N. P., and Marlin, D. H., "Time-Domain Modeling of the Acoustic Impedance of Porous Surface," *Acta Acustica United with Acustica*, Vol. 92, No. 6, 2006, pp. 965–975.

[13] Ostashev, V. E., Collier, S. L., Wilson, D. K., Aldridge, D. F., Symons, N. P., and Marlin, D. H., "Padé Approximation in Time-Domain Boundary Conditions of Porous Surfaces," *Journal of the Acoustical Society of America*, Vol. 122, No. 1, 2007, pp. 107–112. doi:10.1121/1.2743153

[14] Luebbers, R. J., and Hunsberger, F., "FDTD for *N*th-Order Dispersive Media," *IEEE Transactions on Antennas and Propagation*, Vol. 40, No. 11, 1992, pp. 1297–1301. doi:10.1109/8.202707

[15] Cotté, B., and Blanc-Benon, P., "Time-Domain Simulations of Sound Propagation in a Stratified Atmosphere over an Impedance Ground," *Journal of the Acoustical Society of America*, Vol. 125, No. 5, 2009, pp. 202–207. doi:10.1121/1.3104633

[16] Rasmussen, K. B., "Sound Propagation over Grass Covered Ground," *Journal of Sound and Vibration*, Vol. 78, No. 2, 1981, pp. 247–255. doi:10.1016/S0022-460X(81)80036-3

[17] Ostashev, V. E., Wilson, D. K., Liu, L., Aldridge, D. F., Symons, N. P., and Marlin, D., "Equations for Finite-Difference, Time-Domain Simulation of Sound Propagation in Moving Inhomogeneous Media and Numerical Implementation," *Journal of the Acoustical Society of America*, Vol. 117, No. 2, 2005, pp. 503–517. doi:10.1121/1.1841531

[18] Bogey, C., and Bailly, C., "A Family of Low Dispersive and Low Dissipative Explicit Schemes for Flow and Noise Computations," *Journal of Computational Physics*, Vol. 194, No. 1, 2004, pp. 194–214. doi:10.1016/j.jcp.2003.09.003

[19] Berland, J., Bogey, C., and Bailly, C., "Low-Dissipation and Low-Dispersion Fourth-Order Runge–Kutta Algorithm," *Computers and Fluids*, Vol. 35, No. 10, 2006, pp. 1459–1463. doi:10.1016/j.compfluid.2005.04.003

[20] Berland, J., Bogey, C., Marsden, O., and Bailly, C., "High Order, Low Dispersive and Low Dissipative Explicit Schemes for Multiple-Scale and Boundary Problems," *Journal of Computational Physics*, Vol. 224, No. 2, 2007, pp. 637–662. doi:10.1016/j.jcp.2006.10.017

[21] Bogey, C., Caqueray, N., and Bailly, C., "A Shock-Capturing Methodology Based on Adaptative Spatial Filtering for High-Order Non-Linear Computations," *Journal of Computational Physics*, Vol. 228, No. 5, 2009, pp. 1447–1465. doi:10.1016/j.jcp.2008.10.042

[22] Cotté, B., "Propagation Acoustique en Milieu Extérieur Complexe: Problèmes Spécifiques au Ferroviaire Dans le Contexte des Trains à Grande Vitesse.," Ph.D. Thesis, École Centrale de Lyon, No. 2008-19, Écully, France, 2008.

[23] Tam, C. K. W., and Dong, Z., "Radiation and Outflow Boundary Conditions for Direct Computation of Acoustic and Flow Disturbances in a Nonuniform Mean Flow," *Journal of Computational Acoustics*, Vol. 4, No. 2, 1996, pp. 175–201. doi:10.1142/S0218396X96000040

[24] Morse, P. M., and Feshbach, H., *Methods of Theoretical Physics*, Vol. 1, McGraw–Hill, New York, 1953, pp. 370–373.

[25] Embleton, T. F. W., "Tutorial on Sound Propagation Outdoors," *Journal of the Acoustical Society of America*, Vol. 100, No. 1, 1996, pp. 31–48. doi:10.1121/1.415879

[26] Albert, D. G., and Orcutt, J. A., "Acoustic Pulse Propagation Above Grassland and Snow: Comparison of Theoretical and Experimental Waveforms," *Journal of the Acoustical Society of America*, Vol. 87, No. 1, 1990, pp. 93–100. doi:10.1121/1.398917

[27] Tam, C. K. W., and Webb, J. C., "Dispersion-Relation Preserving Finite Difference Schemes for Computational Acoustics," *Journal of Computational Physics*, Vol. 107, No. 2, 1993, pp. 262–281. doi:10.1006/jcph.1993.1142

[28] Attenborough, K., "Sound Propagation Close to the Ground," *Annual Review of Fluid Mechanics*, Vol. 34, 2002, pp. 51–82. doi:10.1146/annurev.fluid.34.081701.143541

[29] Waxler, R., Gilbert, K. E., and Talmadge, C., "A Theoretical Treatment of the Long Range Propagation of Impulsive Signals Under Strongly Ducted Nocturnal Conditions," *Journal of the Acoustical Society of America*, Vol. 124, No. 5, 2008, pp. 2742–2754. doi:10.1121/1.2980520

[30] Zorumski, W., and Willshire, W., "Downwind Sound Propagation in an Atmospheric Boundary Layer," *AIAA Journal*, Vol. 27, No. 5, 1989, pp. 515–523. doi:10.2514/3.10141

[31] Albert, D. G., "Observations of Acoustic Surface Waves in Outdoor Sound Propagation," *Journal of the Acoustical Society of America*, Vol. 113, No. 5, 2003, pp. 2495–2500. doi:10.1121/1.1559191

[32] Chandler-Wilde, S. N., and Hothersall, D. C., "A Uniformly Valid Far-Field Asymptotic Expansion of the Green Function for Two-Dimensional Propagation Above a Homogeneous Impedance Plane," *Journal of Sound and Vibration*, Vol. 182, No. 5, 1995, pp. 665–675. doi:10.1006/jsvi.1995.0225

[33] Enflo, B. O., and Enflo, P. H., "Sound Wave Propagation from a Point Source over a Homogeneous Surface and over a Surface with an Impedance Discontinuity," *Journal of the Acoustical Society of America*, Vol. 82, No. 6, 1987, pp. 2123–2134. doi:10.1121/1.395657

[34] Di, X., and Gilbert, K. E., "An Exact Laplace Transform Formulation for a Point Source Above a Ground Surface," *Journal of the Acoustical Society of America*, Vol. 93, No. 2, 1993, pp. 714–720. doi:10.1121/1.405435

[35] Brekhovskikh, L., *Waves in Layered Media*, 2nd ed., Academic Press, New York, 1980, pp. 417–418.

[36] Cotté, B., and Blanc-Benon, P., "Outdoor Sound Propagation in the Time Domain Using Linearized Euler Equations with Suitable Impedance Boundary Conditions," *13th International Symposium on Long Range Sound Propagation*, École Centrale de Lyon, Écully, France, 2008, pp. 272–284, http://ncpa.olemiss.edu/LRSP.php [retrieved 2011].

[37] Candel, S., "Numerical Solution of Conservation Equations Arising in Linear Wave Theory: Application to Aeroacoustics," *Journal of Fluid Mechanics*, Vol. 83, No. 3, 1977, pp. 465–493. doi:10.1017/S0022112077001293

F. Ladeinde
Associate Editor